

## A highly ionized stellar bow shock in the Small Magellanic Cloud

WILLIAM J. HENNEY, S. JANE ARTHUR, AND M. VALERDI<sup>1</sup>

<sup>1</sup>*Instituto de Radioastronomía y Astrofísica, Universidad Nacional Autónoma de México, Apartado Postal 3-72, 58090 Morelia, Michoacán, Mexico*

### Abstract

We report the discovery of a parsec-scale stellar bow shock associated with the O2 III(f) star Walborn 3 in the cluster NGC 346 of the Small Magellanic Cloud. The bow shock is most clearly detected in He II and [Ar IV] emission lines but is also seen at mid-infrared wavelengths between 12  $\mu$ m and 24  $\mu$ m.

**Keywords:** Atomic physics; Circumstellar matter; Stars: winds, outflows

### 1. INTRODUCTION

The interaction of a star’s wind with the surrounding medium can result in an arc-shaped circumstellar emission nebula, frequently referred to as a bow shock (Gull & Sofia 1979; van Buren & McCray 1988). Stellar bow shocks are found around a wide variety of different stars, including pre-main sequence stars (Bally & Reipurth 2001; Henney et al. 2013), neutron stars (Cordes et al. 1993), and cool giants and supergiants (Sahai & Chronopoulos 2010; Cox et al. 2012), but they are most commonly associated with hot luminous OB stars (van Buren et al. 1995; Kobulnicky et al. 2016). Bow shocks are most frequently observed via their infrared continuum emission (Meyer et al. 2016), which arises from dust grains that are heated by the stellar radiation field (Draine & Li 2007), but specific classes of bow shock have also been identified via multiple thermal and non-thermal emission mechanisms that trace gas and plasma components. The emission arcs are most commonly interpreted as due to the hydrodynamic interaction induced by supersonic relative motion of the star with respect to the ambient material (Wilkin 1996), but models involving a subsonic interaction have also been proposed (Mackey et al. 2015, 2016). Also, the role of the stellar wind ram pressure in supporting the arc may be replaced by radiation pressure in some cases, see Henney & Arthur (2019a,b,c).

Stellar bow shocks can be used to estimate stellar wind mass loss rates by applying momentum-balance arguments (Gvaramadze et al. 2012; Kobulnicky et al. 2018, 2019; Henney & Arthur 2019c). These provide an important check on more traditional spectroscopic methods (Hillier 2020), since the systematic uncertainties and biases are different. Line-

driven wind theory for hot stars predicts that momentum-loss rates should increase with metallicity,  $Z$ , as  $\dot{M}V_w \propto Z^n$  with  $n = 0.6\text{--}0.8$  (Vink et al. 2001; Krtićka & Kubát 2018; Vink & Sander 2021; Björklund et al. 2021) for the most luminous stars ( $L > 10^6 L_\odot$ ).

The closest low-metallicity stellar populations ( $Z = 0.1$  to  $0.2Z_\odot$ , Narloch et al. 2021) are found in the Small Magellanic Cloud (SMC) at a distance of 62 kpc (Graczyk et al. 2020). A small number of stellar bow shocks have been previously identified in the SMC (Gvaramadze et al. 2011; Sheets et al. 2013) by means of their mid-infrared dust emission. The majority of these sources are found far from the cores of dense clusters and are probably *runaways* (Blaauw 1961), which have been ejected from a binary system or stellar cluster (Hoogerwerf et al. 2001; Renzo et al. 2019). In the Milky Way, a second class of stellar bow shocks are found inside young massive star clusters: *weather vanes* (Povich et al. 2008), which have low space velocities and are interacting with streaming motions of the local interstellar medium, such as champagne flows (Tenorio-Tagle 1979).

In this paper, we report the discovery of just such a bow shock inside the massive stellar cluster NGC 346, which excites the H II region N66 (Henize 1956). The bow shock is associated with the very early-type star Walborn 3 (W 3) (Walborn & Blades 1986), also known as MPG 355 (Massey et al. 1989) with spectral type ON2 III(f\*) (Heydari-Malayeri & Selier 2010).

Atmosphere models of Rivero González et al. (2012)

### 2. OBSERVATIONS

The main observational data used in this paper comprise an archival integral field spectral cube of NGC 346 obtained with the MUSE spectrograph (Bacon et al. 2010, 2014) on the VLT as part of program 098.D-0211(A) (PI: W.-R. Hamann). The field of view is 60 arcsec times 60 arcsec with spaxel size

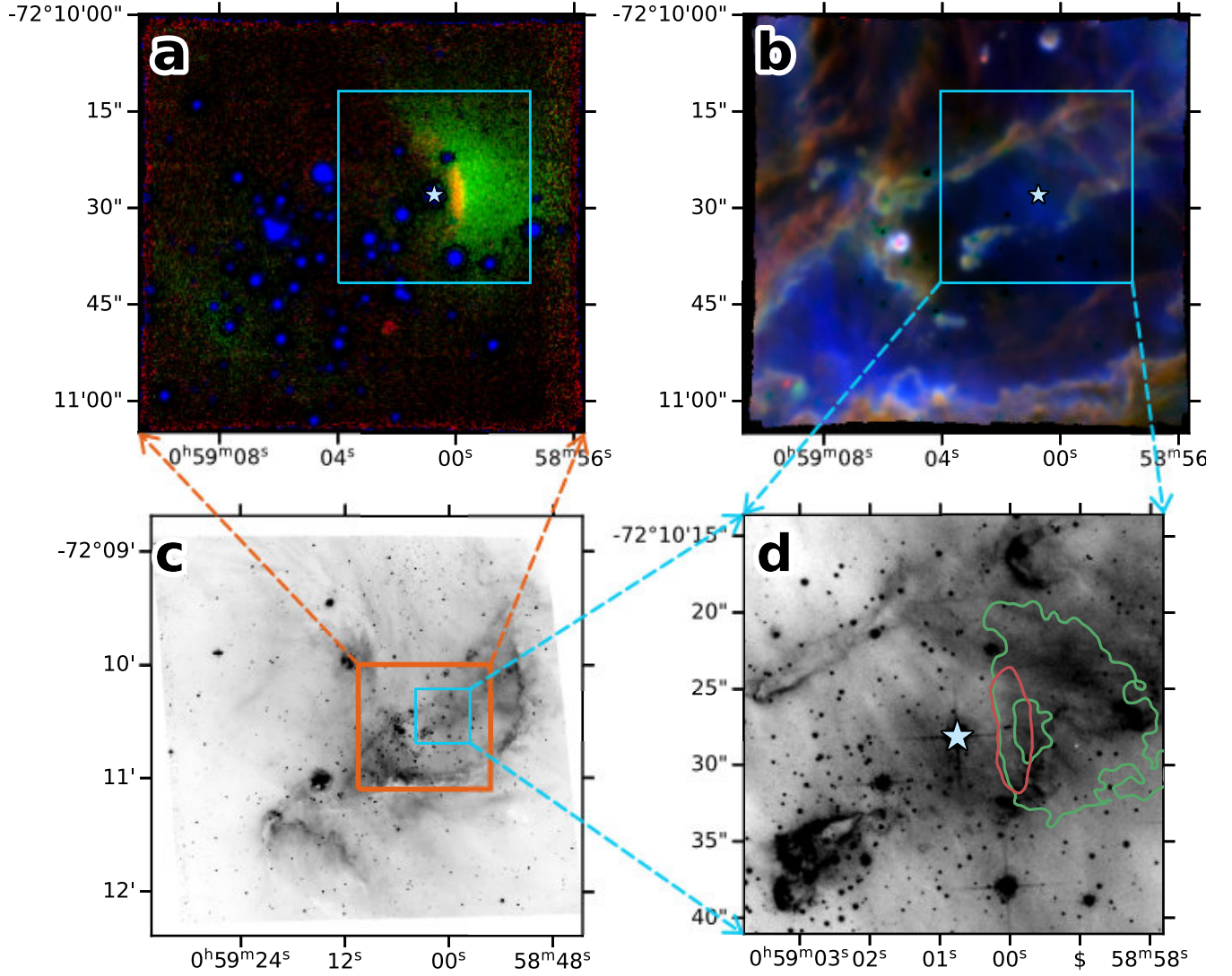


**Figure 1.** MUSE emission line images of the core of NGC 346. (a) High-ionization emission from the bow shock. Red shows He II  $\lambda 4686$ , green shows [Ar IV]  $\lambda 4741$ , blue shows continuum emission at  $4700 \text{ \AA}$  (mainly starlight). The white star indicates the position of W 2. (b) Medium to low-ionization emission from the surrounding H II region. Red shows [O I]  $\lambda 6300$ , green shows [S II]  $\lambda 6731$ , blue shows [S III]  $\lambda 9069$  (c) Location of the MUSE field within the wider nebula against a background  $H\alpha$  image from HST-ACS in the F658N filter (d) Zoom of panel c showing detail of the bow shock region in the light of  $H\alpha$  emission, with superimposed contours of He II (red) and [Ar IV] (green).

of  $0.2 \text{ arcsec}$  and estimated seeing full-width half maximum (FWHM) width of  $0.961 \text{ arcsec}$ . The spectral range is  $4595 \text{ \AA}$  to  $9366 \text{ \AA}$  sampled at  $1.25 \text{ \AA pix}^{-1}$  and the spectral resolving power varies from  $R \approx 2000$  in the blue to  $R \approx 4000$  in the red. We use reduced data from the standard ESO pipeline processing (Weilbacher et al. 2020), co-added across multiple observations obtained on 2016-08-22 with a total effective exposure time of  $12600 \text{ s}$ .

We divide the spectral range into sections of width  $800 \text{ \AA}$  and fit a 6th order polynomial to the continuum in line-free wavelengths of each section, using an independent fit for each spaxel. We then extract individual emission lines (or close blends) from the continuum-subtracted spectra using

$5 \text{ \AA}$  windows, centered on the expected wavelength of each line in the systemic frame of the nebula (heliocentric velocity  $V \approx 160 \text{ km s}^{-1}$ ). We correct for an over-subtraction of the sky background, which is apparent in the pipeline-processed data cube. We establish accurate zero points for all lines by checking that multiple line ratios tend towards physically reasonable asymptotes as the brightness tends towards zero.

We use the observed Balmer decrement between  $H\alpha$  and  $H\beta$  to correct all lines for foreground dust extinction, assuming an SMC-appropriate reddening law with  $R_V = 2.74$  (Fitzpatrick & Massa 1990; Bouret et al. 2003).

### 3. RESULTS

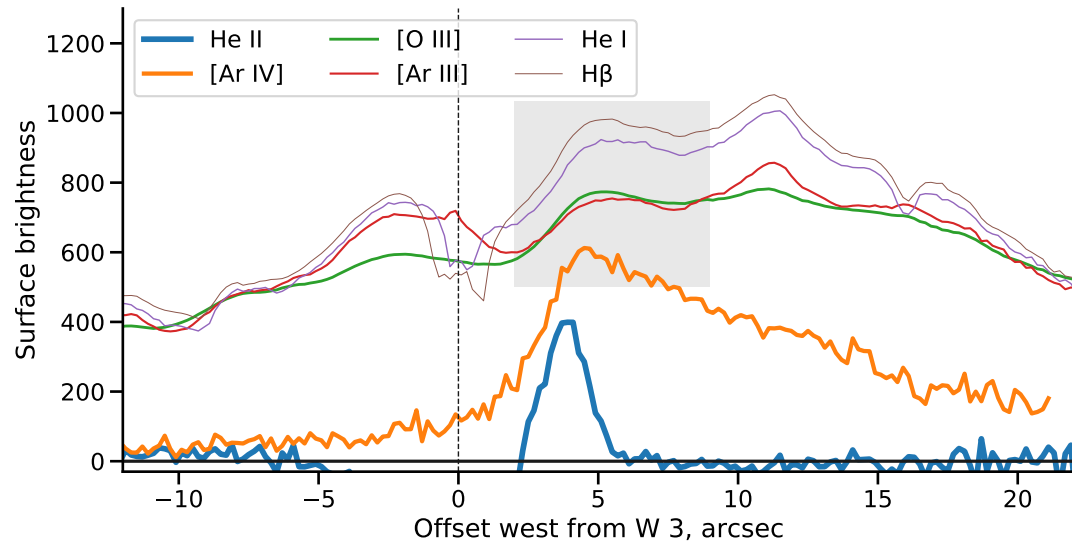


**Figure 2.** Emission line surface brightness profiles along an East–West cut across the bow shock, derived from MUSE integral field spectra.

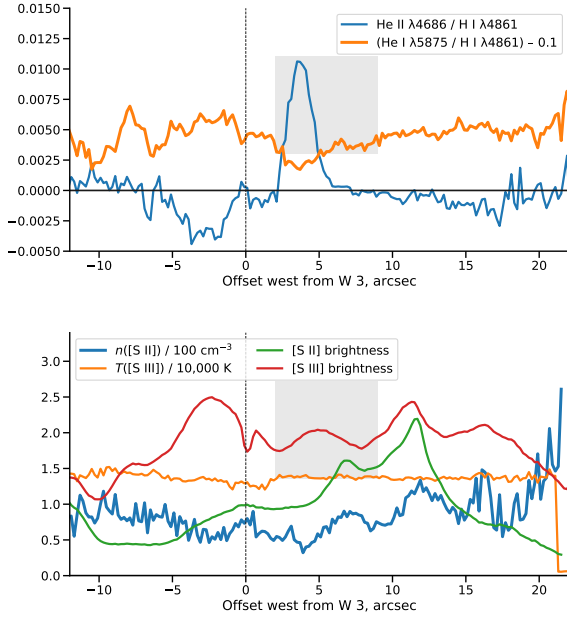


Figure 3. More profiles

An east-facing bow shock structure is detected around the star Walborn 2, as illustrated in Figure 1a. The inner edge of the bow shock is traced by a sharp ridge of He II  $\lambda 4686$  emission (red), while [Ar IV]  $\lambda 4741$  emission (green) is more extended with a diffuse outer boundary. Nebular emission of the same field in moderate and low ionization lines is shown in Figure 1b and there is no evidence of the bow shock in these lines. Instead, the low ionization lines ([O I], red, and [S II], green) trace the ionization fronts at the surface of dense filaments and globules, while the moderate ionization line ([S III], blue) traces diffuse ionized gas in the interior of the nebula that is largely unrelated to the bow shock.

Figure 1c shows the position of the MUSE field (orange box) on a wider scale *HST* image of the N66 H II region (Nota et al. 2006). The head of the bow shock is oriented towards the bright filament outside of the MUSE field to the West, which represents a large scale ionization front at the edge of the H II region.

Figure 1d shows a zoomed view of the *HST*  $H\alpha$  image around W 2, compared with contours of the bow shock emission. The  $H\alpha$  brightness does appear to be slightly higher within the bow shock contours than just outside it, but the ef-

fect is very subtle compared with larger unrelated variations in the  $H\alpha$  brightness.

#### 4. MID-INFRARED EMISSION FROM THE BOW SHOCK

#### 5. LONGSLIT OBSERVATIONS

Apart from the inner rim of the bow shock, there is no diffuse He II emission in the core of NGC 346, or in the

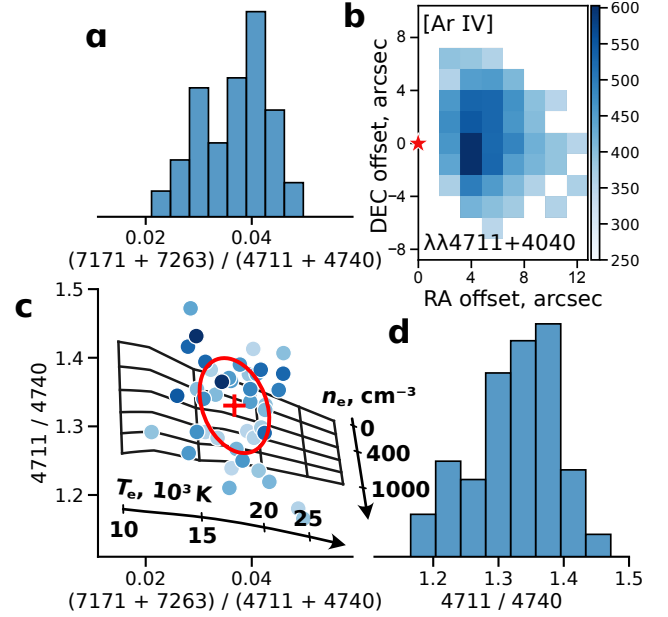


Figure 4. Temperature and density diagnostics of the bow shock from [Ar IV] line ratios.

western side of the N66 region. The eastern side of N66, on the other hand, shows extensive He II  $\lambda 4686$  emission, as can be seen at offsets from  $-200$  to  $-50$  arcsec in Figure 8b. The eastern side of N66 also shows a ten times higher [Fe III] /  $H\beta$  ratio and disturbed kinematics in low-ionization lines such as [S II]. All these are probably due to a foreground supernova remnant SNR B0057–72.2 (Ye et al. 1991) that overlaps with this part of the nebula (Chu & Kennicutt 1988; Nazé et al. 2002; Danforth et al. 2003).

#### 6. CONCLUSIONS

Thank you.

*Facilities:* VLT:Yepun (MUSE)

#### REFERENCES

- Bacon, R., Accardo, M., Adjali, L., et al. 2010, in Society of Photo-Optical Instrumentation Engineers (SPIE) Conference Series, Vol. 7735, Proc. SPIE, 773508, doi: [10.1117/12.856027](https://doi.org/10.1117/12.856027)
- Bacon, R., Vernet, J., Borisova, E., et al. 2014, The Messenger, 157, 13
- Bally, J., & Reipurth, B. 2001, ApJ, 546, 299



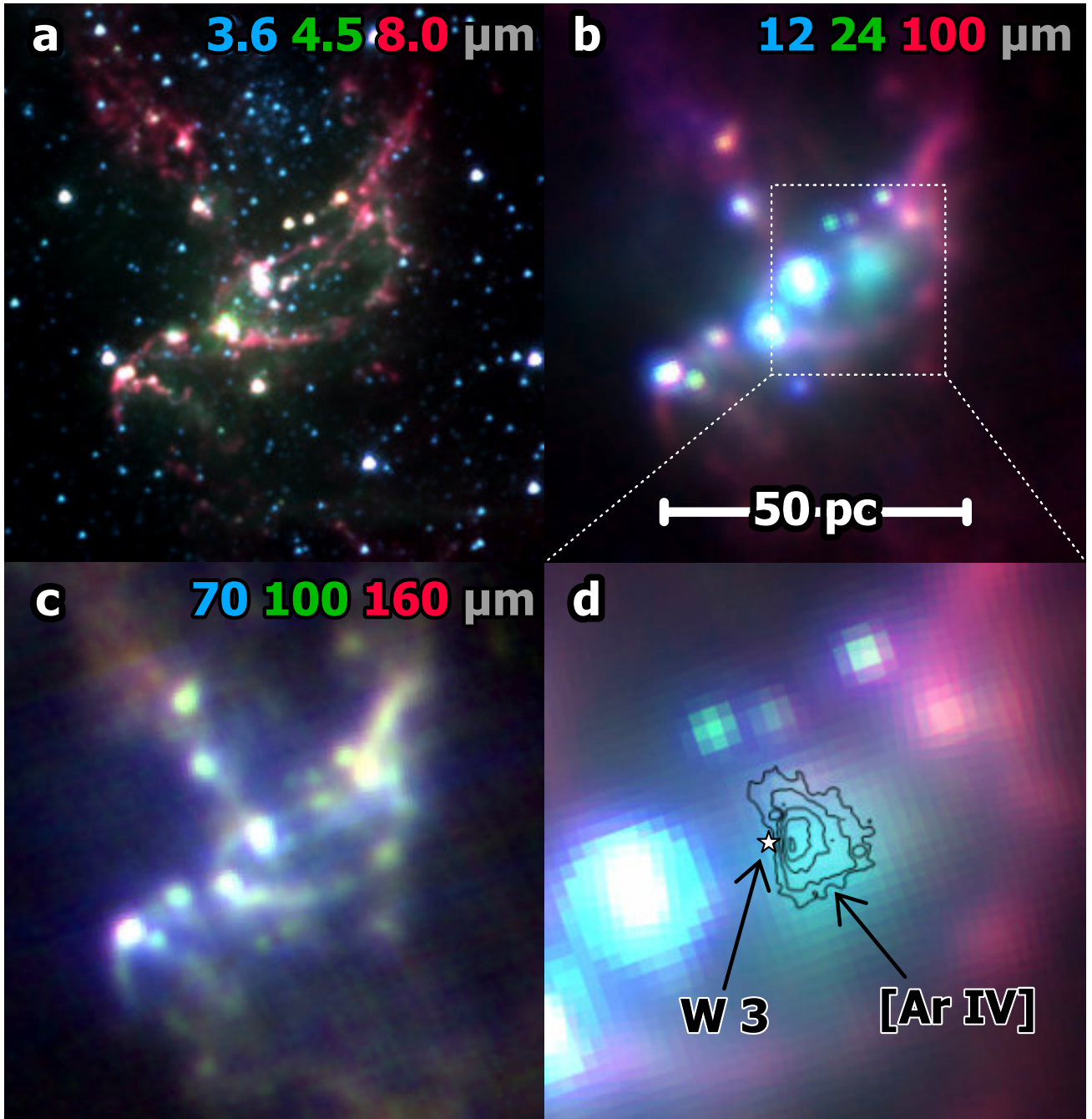


**Figure 5.** Panoramic view of the NGC 346/N66 region at infrared wavelengths: (a) Short wavelength mid-infrared (3.6 to 8 μm); (b) Longer wavelength mid-infrared (12 to 100 μm); (c) Far-infrared (70 to 150 μm); (d) Zoomed view of panel b. Images are from satellite observatories as follows: *Spitzer* IRAC 3.6, 4.5, 8 μm; *WISE* 12 μm; *Spitzer* MIPS 24, 70 μm; *Herschel* PACS 100, 150 μm.

Björklund, R., Sundqvist, J. O., Puls, J., & Najarro, F. 2021, *A&A*, 648, A36

Blaauw, A. 1961, *BAN*, 15, 265

Bouret, J. C., Lanz, T., Hillier, D. J., et al. 2003, *ApJ*, 594, 279, doi: [10.1086/376774](https://doi.org/10.1086/376774)

Chu, Y.-H., & Kennicutt, Robert C., J. 1988, *AJ*, 95, 1111

Cordes, J. M., Romani, R. W., & Lundgren, S. C. 1993, *Nature*, 362, 133

Cox, N. L. J., Kerschbaum, F., van Marle, A.-J., et al. 2012, *A&A*, 537, A35

Danforth, C. W., Sankrit, R., Blair, W. P., Howk, J. C., & Chu, Y.-H. 2003, *ApJ*, 586, 1179

Draine, B. T., & Li, A. 2007, *ApJ*, 657, 810

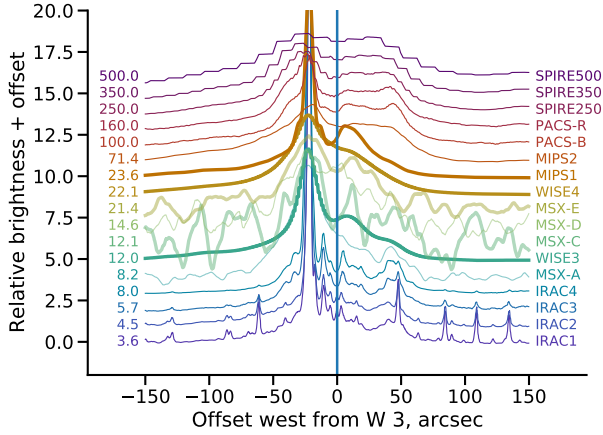


**Figure 6.** East-west brightness profile cuts in various infrared bands.

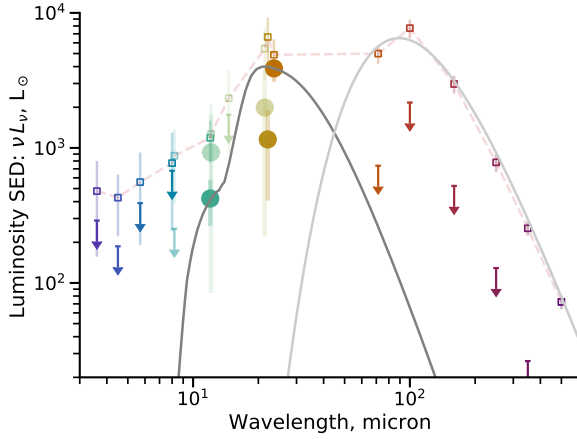


**Figure 7.** Spectral energy distribution of bow shock (large symbols and downward arrows) and background nebula small symbols joined by dashed line.

Fitzpatrick, E. L., & Massa, D. 1990, *ApJS*, 72, 163,  
doi: [10.1086/191413](https://doi.org/10.1086/191413)

Graczyk, D., Pietrzyński, G., Thompson, I. B., et al. 2020, *ApJ*,  
904, 13

Gull, T. R., & Sofia, S. 1979, *ApJ*, 230, 782

Gvaramadze, V. V., Langer, N., & Mackey, J. 2012, *MNRAS*, 427,  
L50

Gvaramadze, V. V., Pflamm-Altenburg, J., & Kroupa, P. 2011,  
*A&A*, 525, A17

Henize, K. G. 1956, *ApJS*, 2, 315

Henney, W. J., & Arthur, S. J. 2019a, *MNRAS*, 486, 3423

—. 2019b, *MNRAS*, 486, 4423

—. 2019c, *MNRAS*, 489, 2142

Henney, W. J., García-Díaz, M. T., O'Dell, C. R., & Rubin, R. H.  
2013, *MNRAS*, 428, 691

Heydari-Malayeri, M., & Selier, R. 2010, *A&A*, 517, A39

Hillier, D. J. 2020, *Galaxies*, 8, 60

Hoogerwerf, R., de Bruijne, J. H. J., & de Zeeuw, P. T. 2001, *A&A*,  
365, 49

Kobulnicky, H. A., Chick, W. T., & Povich, M. S. 2018, *ApJ*, 856,  
74 (K18)

—. 2019, *AJ*, 158, 73

Kobulnicky, H. A., Chick, W. T., Schurhammer, D. P., et al. 2016,  
*ApJS*, 227, 18

Krtićka, J., & Kubát, J. 2018, *A&A*, 612, A20

Mackey, J., Gvaramadze, V. V., Mohamed, S., & Langer, N. 2015,  
*A&A*, 573, A10

Mackey, J., Haworth, T. J., Gvaramadze, V. V., et al. 2016, *A&A*,  
586, A114

Massey, P., Parker, J. W., & Garmany, C. D. 1989, *AJ*, 98, 1305

Meyer, D. M.-A., van Marle, A.-J., Kuiper, R., & Kley, W. 2016,  
*MNRAS*, 459, 1146

Narloch, W., Pietrzyński, G., Gieren, W., et al. 2021, *A&A*, 647,  
A135

Nazé, Y., Hartwell, J. M., Stevens, I. R., et al. 2002, *ApJ*, 580, 225

Nota, A., Sirianni, M., Sabbi, E., et al. 2006, *ApJL*, 640, L29,  
doi: [10.1086/503301](https://doi.org/10.1086/503301)

Povich, M. S., Benjamin, R. A., Whitney, B. A., et al. 2008, *ApJ*,  
689, 242

Renzo, M., Zapartas, E., de Mink, S. E., et al. 2019, *A&A*, 624,  
A66

Rivero González, J. G., Puls, J., Massey, P., & Najarro, F. 2012,  
*A&A*, 543, A95

Sahai, R., & Chronopoulos, C. K. 2010, *ApJL*, 711, L53

Sheets, H. A., Bolatto, A. D., van Loon, J. T., et al. 2013, *ApJ*, 771,  
111

Tenorio-Tagle, G. 1979, *A&A*, 71, 59

van Buren, D., & McCray, R. 1988, *ApJL*, 329, L93

van Buren, D., Noriega-Crespo, A., & Dgani, R. 1995, *AJ*, 110,  
2914

Vink, J. S., de Koter, A., & Lamers, H. J. G. L. M. 2001, *A&A*,  
369, 574

Vink, J. S., & Sander, A. A. C. 2021, *MNRAS*, 504, 2051

Walborn, N. R., & Blades, J. C. 1986, *ApJL*, 304, L17

Weilbacher, P. M., Palsa, R., Streicher, O., et al. 2020, *A&A*, 641,  
A28, doi: [10.1051/0004-6361/202037855](https://doi.org/10.1051/0004-6361/202037855)

Wilkin, F. P. 1996, *ApJL*, 459, L31

Ye, T., Turtle, A. J., & Kennicutt, R. C., J. 1991, *MNRAS*, 249, 722

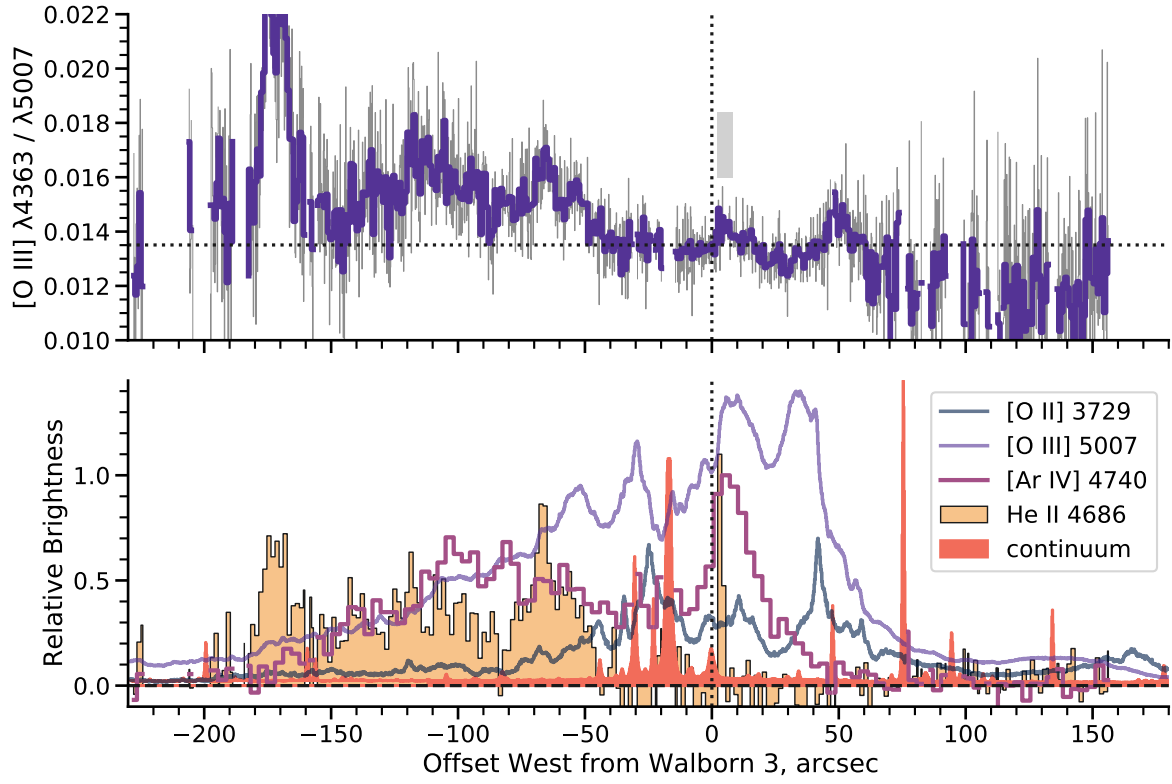


**Figure 8.** Emission line surface brightness profiles and line ratios along a large-scale East–West cut across the entire region, based on FORS1 longslit spectra. The slit is close to the symmetry axis of the bow shock. (a) Temperature-sensitive line ratio  $[O\ III] \lambda 4363 / \lambda 5007$ . The gray box shows the same inner rim region of the bow shock that is highlighted by a gray box in Fig. 2. (b) Selected emission lines from a wide range of ionization stages.

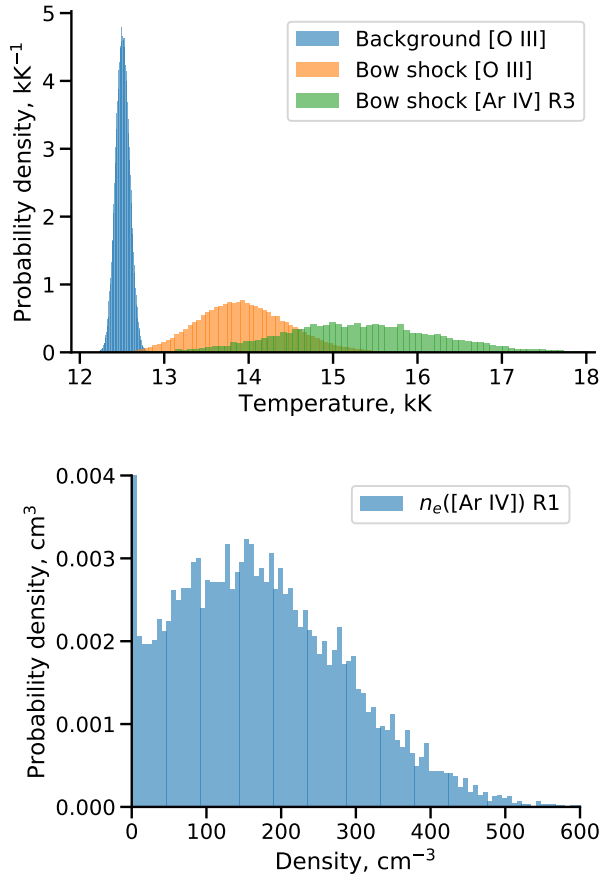


**Figure 9.** Derived temperature of nebula and bow shock.